Proceedings of ASME Turbo Expo 2011
GT2011
June 6-10, 2011, Vancouver, British Columbia, Canada

GT2011-46499

THERMAL PERFORMANCE OF A BUMP TYPE GAS FOIL BEARING FLOATING ON A HOLLOW SHAFT FOR INCREASING ROTATING SPEED AND STATIC LOAD

Kyuho Sim Postdoctoral Research Associate
Jin Woo Song Research Assistant
Yong-Bok Lee Principal Research Scientist
Tae Ho Kim Senior Research Scientist

Energy Mechanics Center, Korea Institute of Science and Technology
39-1 Hawolgok-dong, Songbuk-gu, Seoul, Korea, 136-791

ABSTRACT

Identifying thermal characteristics of gas foil bearings (GFBs) provides an insight for successful implementation into high speed oil-free turbomachinery. The paper presents temperature measurements of a bump type GFB floating on a hollow shaft for various operating conditions. Two angular ball bearings support the hollow shaft at one end (right), and the other end (left) is free. Test GFB has the outer diameter of 100 mm and the axial length of 45 mm, and the hollow shaft has the outer and inner diameters of 60 mm and 40 mm, respectively. An electric motor drives the hollow shaft using a spline coupling connection. A mechanical loading device provides static loads on test GFB upward via a metal wire, and a strain gauge type load cell placed in the middle of the wire indicates the applied loads. During experiments for shaft speeds of 5 krpm, 10 krpm, and 15 krpm and with static loads of 58.86 N (6 kg_f), 78.48 N (8 kg_f), and 98.1 N (10 kg_f), twelve thermocouples measure the outer surface temperatures of test GFB at four angular locations of 45 deg, 135 deg, 215 deg, and 315 deg, with an origin at the top foil free end, and three axial locations of bearing centerline and both side edges at each angle. Two infrared thermometers measure the outer surface temperature of the hollow shaft at free and supported ends close to test GFB. Test results show that GFB temperatures increase as the shaft speed increases and as the static load increases, with higher temperatures in the loading zone (135 deg and 215 deg) than those in the unloading zone (45 deg and 315 deg). In general, the recorded temperatures are highest at 225 deg where a highest hydrodynamic pressure is expected to build up. Measured temperatures at the bearing centerline are higher than those at the side edges, as expected. In addition, large thermal gradients are recorded in the hollow shaft along the axial direction with higher temperatures at the supported end. Angular ball bearings and lip seal supporting the hollow shaft might produce significant heat generation due to mechanical contact as the shaft speed increases. The axial thermal gradient of the shaft is thought to cause higher temperatures at the bearing right edge facing the ball bearing support than those at the left edge. The present test data along with detailed test GFB/shaft geometries and material properties benchmark thermohydrodynamic (THD) model predictions of test GFB with a rotating hollow shaft.

INTRODUCTION

Gas foil bearings (GFBs) have been widespread in various high speed and high temperature rotating machinery due to the enhanced rotordynamic performance at high speeds and the capability of accommodation of thermal deformations at high temperatures [1]. A bump type GFB comprises top and bump foils between its journal and bearing housing. The top foil forms a smooth bearing surface for hydrodynamic pressure generations. The bump foil acting as an elastic foundation yields a broad minimum film thickness region, thus producing enhanced load capacity [2]. GFBs have many other advantages such as simple design, light weight, and low power loss.

Recently, GFBs are used in high (or moderately high) temperature applications, such as high speed/power electric motor, turbo blower/compressor, and micro gas turbines, to name a few. The high temperature applications require adequate thermal management of GFBs because the radial thermal expansions of the shaft can exceed thin film thickness, i.e., thermal seizure or failure [3]. The static and dynamic performances of GFBs also vary considerably at high temperatures. However, the analysis of thermal effects is still challenging because typical GFBs are composed of many subcomponents and have a complicated thermal phenomenon around its foil structure. Moreover, the analysis requires a thermal model including all the thermal paths within and around the system for a complete solution. Therefore, the studies of thermal effects on GFBs have been mainly focused on experimental studies.

In 1998, DellaCorte [4] proposes a test rig for high temperature operation of GFBs to measure bearing performance and durability. The test rig operates up to 70 krpm and 700 °C. The spindle is driven by an impulse air turbine and supported by two angular ball bearings, sustaining up to 500 N. A test GFB is placed at the opposite end of the turbine with a furnace enclosed. A torque rod, which is connected to a force transducer, is attached to the top of the bearing housing. A pneumatic load cylinder is connected to the bottom of the bearing housing in series with a load cell to apply static loads. Bearing torque (or power loss) is measured as a function of speed and load. The results show a typical behavior of fluid film journal bearings, i.e. approximately proportional increase of torque to speed and load. At a high temperature of 537 °C, the overall bearing torque reduces by ~50% when compared to that at 25 °C.

In 2000, Dellacorte et al. [5] investigates the performance and durability of GFBs at temperatures from 25 °C to 650 °C under a wide range of loads, using the test rig in Ref. [4]. The experimental data show that bearing torque is proportional to the static load, and shifts down at increasing temperatures. The least square fit of measured friction force versus static load provides useful information about bearing friction coefficient and preload: the slope of the least square fit implies a friction coefficient and the intersection to the y axis (friction force at zero load) indicates a preload. The authors conclude that at higher temperatures, the decrease of friction coefficient leads to the reduction of friction force, and the thermal expansion of the shaft causes the increase of preload. However, the effect of the journal surface solid lubricant coating on the reduction of friction coefficient is not accounted for. Moreover, the effect of thermal expansion, i.e., clearance change, is estimated without measuring or predicting specific temperatures of the shaft and bearing housing.

In 2004, Radil and Zeszotek [6] present an experimental investigation into the thermal feature of a 3rd generation GFB with the bearing length of 40.5 mm and the diameter of 50.8 mm by measuring bump temperatures in the loading region (upper half side with a downward loading). Nine thermocouples are routed through access holes into the bearing housing, and welded to the backside of the bump foil. The results show that measured bump temperatures are fairly symmetric about the bearing centerline at 20 krpm. The front temperature in the shaft tip side is slightly lower than the rear, indicating larger heat convection to the ambient on the shaft surfaces. The difference between the front and rear temperatures became larger at a higher speed of 50 krpm. Transient temperature responses at 40krpm with static load increasing from 9 N to 222 N show a stepwise increase reaching the maximum temperature of ~170°C. Overall temperatures show relatively proportional increases with respect to the rotating speed increasing from 20 to 50 krpm and the static load increasing from 9 N to 222 N.

In 2009, Kim et al. [7] investigate into the temperature effects on the static and dynamic performance of a GFB structure with the bearing diameter and length of 38 mm during experimental tests accompanying numerical analyses. The test bearing is heated by a cartridge heater placed inside the shaft. GFB structure deflection versus static load at various temperatures of 22 °C, 89 °C, and 188 °C indicates that the bearing becomes stiffer at large bump deflection, agreeing well with a cubic polynomial fit. The level of bump deflections increases at high temperatures. The authors conclude that the structural softening of the bearing results from the thermal expansion of the bearing housing at high temperatures. Numerical predictions show good agreements to the experiments.

In 2010, Kim and San Andres [8] investigate into the thermal performance of GFBs by thermohydrodynamic (THD) model predictions and experiments with cooling flow effects considered. A dedicated test rig is constructed with two GFBs and a hollow shaft connected to a DC motor by a flexible coupling. A cartridge heater heats the hollow shaft inside. Temperatures are measured inside the bearing housing close to the bump foil at five locations along the circumference at the bearing centerline. The measured temperatures of the bearing housing and shaft show moderate increases upon speed-up to 26 krpm. A cooling flow supplied into the space between two bearings reduces slightly the temperatures. During speed-up and coast-down tests, rotor imbalance response measurements at higher temperatures show decreases of the peak amplitudes and increases of the critical speed, thus evidencing the decrease of the bearing clearance, i.e., the larger temperature rise of the shaft than the housing leads to the reduction of the bearing clearance. However, the study does not account for the effect of static loads on thermal characteristics.

Recently, Lee and Kim [13] present a THD model of GFBs, which is an extension of the THD model of compliant flexure pivot tilting pas gas bearings given in Ref. [9]. Each bump arc from the top foil to the bearing housing in a bump is modeled as a thermal resistance. Heat transfer along the bump channels are solved considering heat convections from the surrounding foil structures and bearing housing. The THD model employs a lumped model for the bearing housing and one dimensional (1-D) heat conduction along the shaft to simplify temperature variations within the bearing housing.

This paper aims to identify thermal characteristics of GFBs for successful implementation into oil-free turbomachinery. Temperatures of a bump type GFB floating on a hollow shaft are measured for various operating conditions: increasing rotating speeds and static loads, and variation of the bearing clearance. The present test data benchmark THD model predictions of test GFBs.

TEST RIG CONFIGURATION

Figure 1 shows a bump-type test GFB with a single top foil and a single bump strip layer (1st generation). The top and bump foils of the test GFB, made from Inconel 750 with the thickness of 0.12 mm, are constructed in the laboratory. The bearing housing made from Inconel 718 with the inner and outer diameters of 61.34 mm and 100 mm holds the foil structure with a screw-type holder. The foil structure and the bearing housing have the axial length of 45 mm. A hollow shaft is made from Inconel 718, and has the inner and outer diameters of 40 mm and 60 mm. Table 1 gives the materials and geometries of the test GFB system.

Figure 2 presents a static load and thermal performance test rig with a bump type GFB floating on a hollow shaft, which is driven by an electric motor. The test rig is composed of 4 parts: a floating GFB, a shaft hollow only in the bearing section, a center-housing for shaft support, and an electric motor. The floating GFB housing has an assembled rod at the upper side for static loading and torque measurement. The center housing has two oil lubricated ball bearings and side end seals to support the test shaft. The figure also shows an installation of two strain gauge type load cells for measurements of static load on test GFB and the bearing friction torque. Two orthogonally positioned fiber optic sensors fixed on the bearing housing measure the relative motions of the bearing housing to the shaft. Twelve K-type thermocouples are attached on the outer surface of the bearing housing, and two noncontact infrared thermometers are installed at the side of the bearing housing to measure the shaft temperatures. Table 1 presents the materials and geometry of the rotor - GFB system.

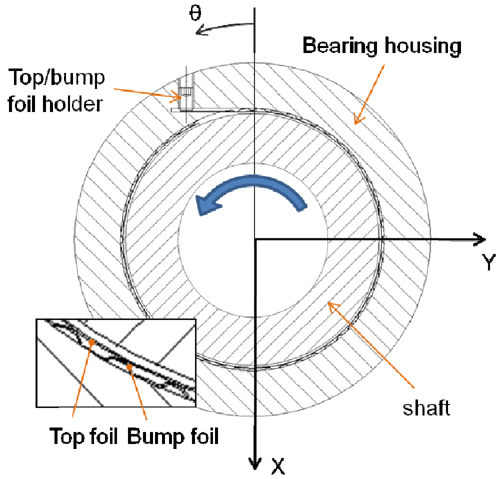

Fig. 1 Bump-type test GFB with a single top foil and a single bump strip layer (1st generation)

Table 1 Materials and Geometries of test GFB (1st generation)

Materials			
Shaft/bearing housing		Inconel 718	
Top/bump/shim foil		Inconel 750	
Geometry		Value	unit
Shaft diameter	Outer	60.00	mm
	Inner	40.00	mm
Housing diameter	Outer	100.0	mm
	Inner	61.34	mm
Bearing length		45.0	mm
Bump pitch		4.3	mm
Bump length		2.3	mm
Bump height		0.4	mm
Bump foil thickness		0.12	mm
Top foil thickness		0.12	mm

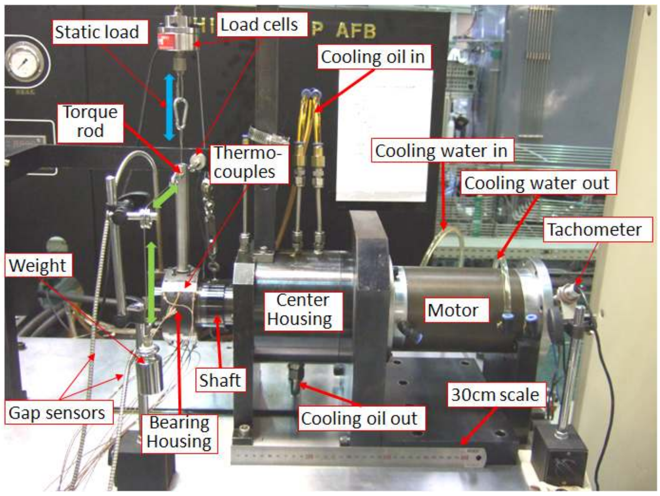

Fig. 2 Static load performance measurement test rig with measurement instruments installed.

GFB DISPLACEMENT VERSUS STATIC LOAD

Figure 3 presents the GFB displacement versus static load recorded during consecutive loading and unloading tests. A 13 kg_f weight is pre-installed to the bearing housing to give an initial negative static load. Static loads are applied to the test GFB by pull and release of a metal wire up to ±13 kg_f. The recorded data shows a typical nonlinearity of the GFB, i.e., relatively soft around the origin and extremely hard at both the displacement limits. A null stiffness region does not exist due to manufacturing inaccuracy. The nominal radial clearance of the test GFB is estimated from the relatively soft range with a radial length of ~70 μm.

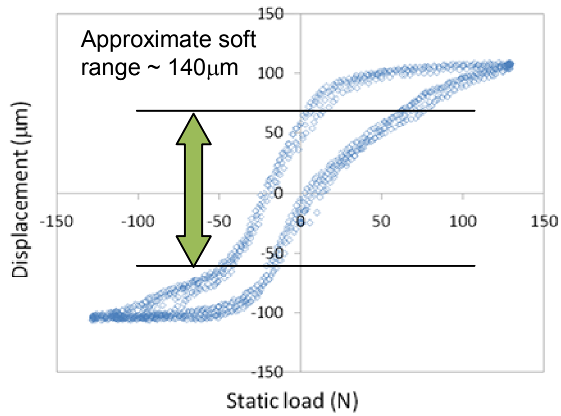

Fig. 3 GFB displacement versus static load recorded during consecutive loading – unloading tests. Estimated nominal radial clearance C_{nom}= 70 μm.

BASELINE SHAFT TEMPERATURE

Figure 4 presents measured baseline shaft temperatures without the test GFB at shaft speeds of 5 krpm, 10 krpm, and 15 krpm. Outer surface temperatures of the shaft are measured at five locations (TR 1~5), evenly distributed along the shaft length, with an infrared thermo-gun to avoid disturbing air flows around the shaft. In the transient temperature responses in Fig. 5(a), with increasing shaft speeds, the shaft temperatures close to the center housing increase significantly up to 60 °C, but those at the free end show relatively limited increases below 35 °C. Most shaft temperatures show temporary drops of ~2°Cright immediately after speed-ups due to increased heat convections at higher shaft speeds, and delayed heat transfer from the center housing. The temporary temperature drop does not appear at TR5 near the center housing because the shaft is not hollow at the position. The measured shaft temperatures at steady state in Fig. 5(b) show strong thermal gradient along the axial length because significant heat generation in the center housing by the mechanical contacts of the lip seal and ball bearing, and strong heat convection at the shaft free end due to the shaft spinning. The temperature difference of 25 °C along the shaft axial length (~75 mm) reveals strong heat convections on the exposed surfaces, inside and outside, of the rotating shaft.

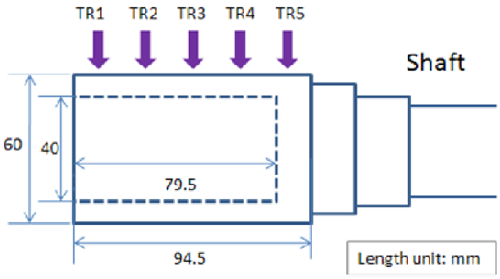

Fig. 4 Temperature measurement locations on shaft. Five locations (TR 1~5) evenly distributed along shaft axial length. Test GFB not installed.

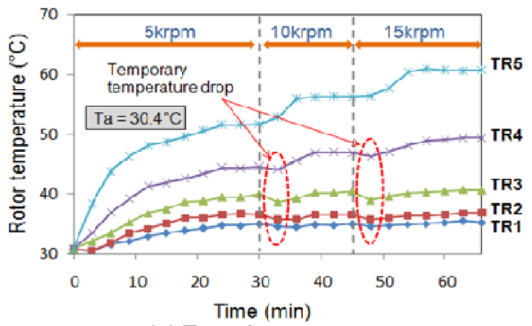

(a) Transient reponses

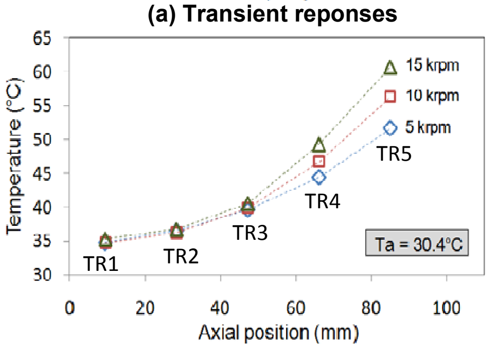

(b) Steady state responses

Fig. 5 Measured shat temperatures at five locations (TR 1~5) on shaft for increasing shaft speed from 5 krpm to 15 krpm. Test GFB not installed.

EXPERIMENTAL TEST RESULTS

Figure 6 illustrates temperature measurement locations on the shaft and bearing housing for rotor spinning tests. Twelve K-type thermocouples measure the outer surface temperatures of test GFB housing at four angular locations of 45 deg, 135 deg, 215 deg, and 315 deg, with an origin at the top foil free end, and three axial locations of the bearing centerline (C) and both the side edges (L: left, R: right). Two noncontact infrared thermometers (TR_L: shaft left end, TR_R: shaft right end) measure the outer surface temperatures of the shaft at a distance of ~10 mm from the test GFB.

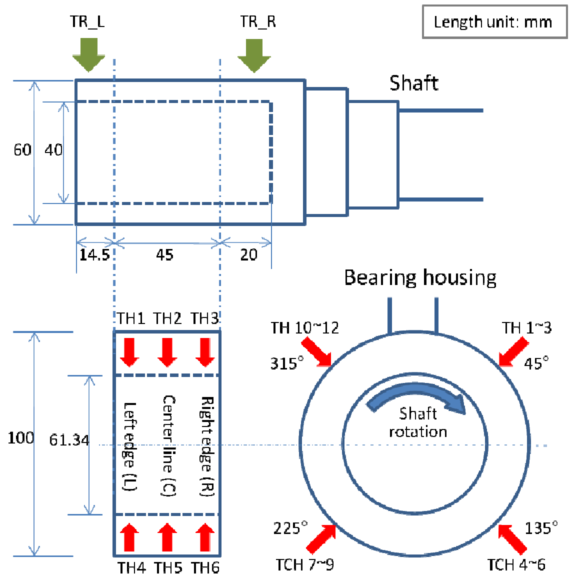

Fig. 6 Temperature measurement locations on shaft and bearing housing. TR_L (shaft left end) and TR_R (shaft right end): noncontact infrared thermometer. TH 1~12: K-type thermocouples on bearing housing outer surface alonog left edge (L), centerline (C), and right (R) edge at circumferential positions of 45 deg, 135 deg, 225 deg, and 315 deg.

Figure 7 presents transient reponses of measured test GFB temperatures for increasing shaft speed from 5 krpm to 15 krpm with static load of 6 kg_f . the nominal radial clearance of test GFB is 70 μm. Note that hereafter the test GFB temperatures represent the measured outer surface temperatures of the test GFB housing. The electric motor starts to drive the shaft at 5 krpm with the static load of 6 kg_f applied, and the shaft speed is maintained until the test GFB temperatures reach a steady state. Then, the speed is increased to the next rotating speed. The steady state test GFB temperatures increase moderately with increasing shaft speeds. The test GFB temperatures decrease slightly immediately after each speed-up, as shown in the baseline shaft temperatures in Fig. 5. The bearing centerline temperatures are higher slightly than those at the side edges, but the differences are small less than 3 °C even at the highest shaft speed due to the relatively small distance of ~20 mm from the centerline to the side measurement locations. The axial temperature differences are larger at the loading zone (135 deg and 215 deg) than at the unloading zone (45 deg and 315 deg) due to more heat dissipations within the air film.

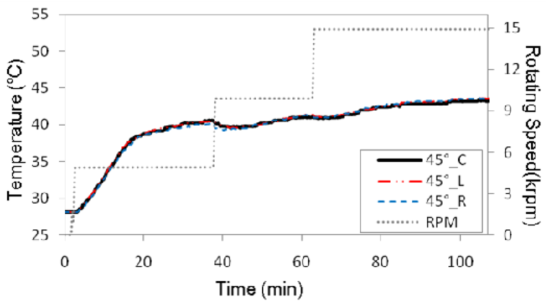

(a) 45 deg (unloading zone)

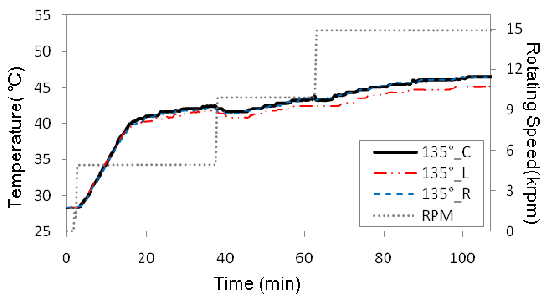

(b) 135 deg (loading zone)

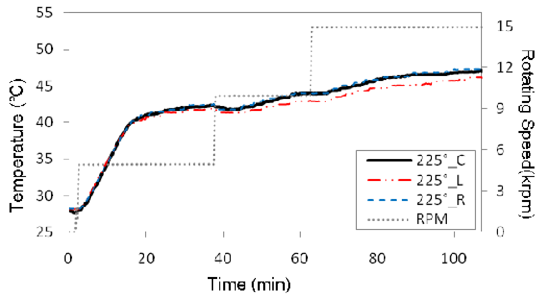

(c) 225 deg (loading zone)

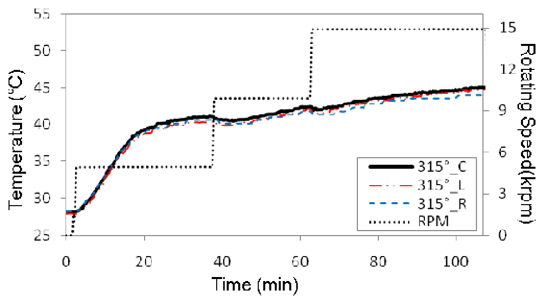

(d) 315 deg (unloading zone)

Fig. 7 Transient reponses of measured temperatures at test GFB housing for increasing shaft speed from 5 krpm to 15 krpm with static load of 6 kgf. Measurements at centerline (C), left end (L), and right end (R). Nominal radial clearance: 70 μm.

Figure 8 presents transient reponses of measured shaft temperatures at left (L) and right (R) ends for increasing shaft speed from 5 krpm to 15 krpm with a static load of 6 kg_f. The right shaft temperature close to the center housing is higher than the left due to heat transfer from the center housing. As the shaft speed increases, the temperature differences become larger due to the stronger heat conveciton on the shaft free left end and more heat flows from the center housing at the right end, showing a similar behavior of the baseline shaft temperatures in Fig. 5. When compared to the baseline shaft temperatures (TR1 and TR5) of 35 °C and 61 °C at 15 krpm, the shaft temperatures of 38 °C and 60 °C at the left and right ends, respectively, imply that the heat generation in the air film with the static load of 6 kg_f is relatively small to change significnatly the thermal feature of the test GFB. Note that the shaft with strong heat convections on the exposed surfaces converges to the steady state faster than the GFB housing, which is in a mild heat convection environment. The GFB temperatures lie between two shaft temperatures, i.e., left and right, but close to the shaft temperature at the left end.

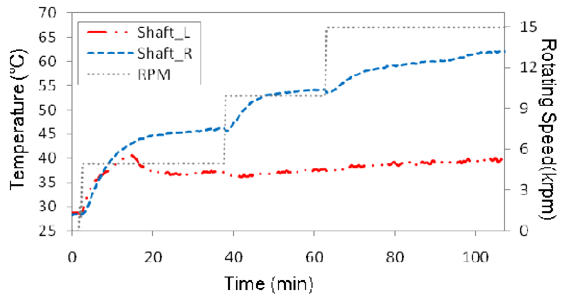

Fig. 8 Transient reponses of measured temperatures at shaft left (L) and right (R) ends for increasing shaft speed from 5 krpm to 15 krpm with static load of 6 kg_f.

Figure 9 shows transient GFB temperature responses at the centerline of 45 deg, 135 deg, 215 deg, and 315 deg with static load of 6 kg_f. The test GFB has higher temperatures in the loading zone (135 deg and 215 deg). The circumferential temperature differences are higher than the axial temperature differences.

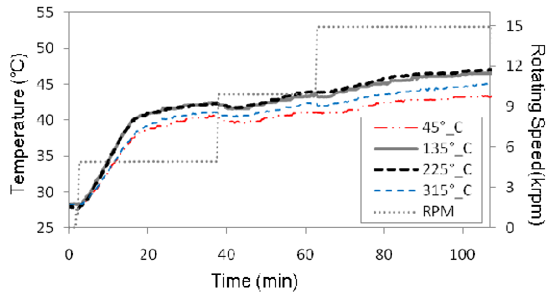

Fig. 9 Transient responses of measured temperatures at test GFB housing centerline (M) for increasing shaft speed from 5 krpm to 15 krpm with static load of 6 kg_f. Nominal radial clearance: 70 μm.

Figure 10 presents the effect of the bearing clearance reduction to 40 μm on the GFB temperatures. Insertion of a shim foil with a thickness of 30 μm between the bump layer and the bearing inner surface decreases the original nominal radial clearance of 70 μm to 40 μm. Test data show that the GFB temperatures increase by ~5 °C at 15 krpm with larger circumferential temperature differences than those in Fig. 9. The results imply the increase in heat generation in the air film. Tables 2 and 3 list the measured steady state GFB temperatures for the nominal radial clearances of 70 μm and 40 μm, respectively, at the bearing centerline (45 deg, 135 deg, 225 deg, and 315 deg) and the shaft at left and right ends for increasing speeds with increasing static loads.

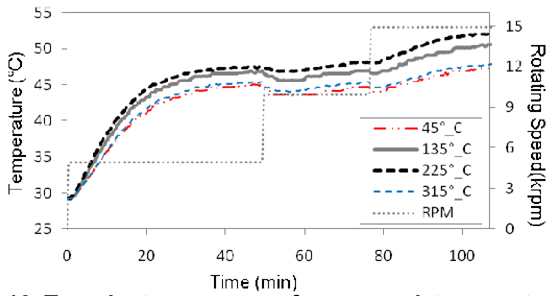

Fig. 10 Transient reponses of measured temperatures at test GFB housing cenerline (M) for increasing shaft speed from 5 krpm to 15 krpm with static load of 6 kg_f. Nominal radial clearance: 40 μm

Table 2 Steady state temperatures of GFB housing at bearing centerline and shaft at left and right ends. Nominal radial clearance: 70 μm (temperature unit: °C).

Speed (krpm)	Load (kg_f)	GFB angular position (deg)				Shaft axial position	
		45	135	225	315	Left	Right
5	6	40.4	42.3	42.3	41.2	37.2	46.0
	8	43.3	45.2	46.2	43.2	39.5	46.0
	10	44.2	46.7	46.8	44.7	40.8	44.8
10	6	41.2	43.6	44.0	42.3	37.7	54.0
	8	42.3	44.4	45.7	42.5	37.7	52.7
	10	45.7	48.0	48.2	45.6	42.4	52.6
15	6	42.5	45.1	46.7	43.3	38.0	60.0
	8	43.6	46.5	47.1	44.9	39.5	62.2
	10	45.4	49.5	49.5	46.7	43.6	59.1

Table 3 Steady state temperatures of GFB housing at bearing centerline and shaft at left and right. Nominal radial clearance: 40 μm (temperature unit: °C).

Speed (krpm)	Load (kg_f)	GFB angular position (deg)				Shaft axial position	
		45	135	225	315	Left	Right
5	6	44.7	46.2	47.6	45.3	43.0	49.8
	8	48.4	50.9	51.7	48.5	45.9	50.3
	10	48.2	49.4	50.2	47.7	44.5	49.5
10	6	44.5	46.8	48.2	45.3	42.5	59.0
	8	45.5	47.7	48.7	45.3	43.5	57.7
	10	47.0	48.7	49.6	46.6	41.8	58.1
15	6	47.2	50.3	52.1	47.9	46.3	68.5
	8	48.2	50.3	52.2	48.1	46.1	67.2
	10	49.4	51.7	53.5	50.1	46.1	68.3

THD MODEL OF TEST GFB (1ST GENERATION)

Figure 11 presents a schematic of the Thermohydrodynamic (THD) model of test GFB, consisting of four sub-systems of the shaft, air film/top foil, bump foil layer, and bearing housing. In the room temperatures, typical heat transfers in the GFB occur from the air film, where heat dissipations occur, to the shaft and the bearing housing via the foil structure, and then to the environments. The hollow shaft is modeled as a two dimensional (2-D) axi-symmetric heat conduction in the axial and radial direction. The air film is governed by the Reynolds equation for a compressible fluid flow and a three dimensional (3-D) energy transport equation, including the top foil in the bearing thermal boundaries. The bump foil layer is modeled as a thermal resistance of heat conduction along the bump arc, allowing heat convections to the bump channels. Lastly, the bearing housing is modeled as a 3-D heat conduction. The four thermal domains are interconnected by the 1st order continuity of temperature at the interfaces between the sub-systems.

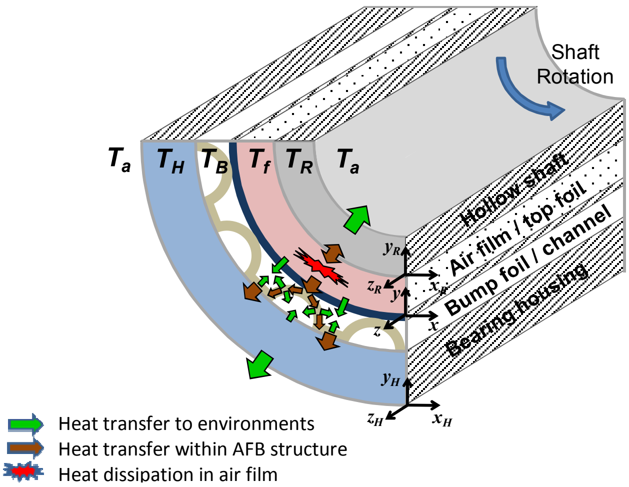

Fig. 11 Schematic view of typical heat transfers in GFBs with viscous heat generation in gas (air) film when cooperating at room temperature. Local coordinates of air film, shaft, and bearing housing are *x-y-z*, x_R-y_R-z_R, and x_H-y_H-z_H, respectively.

The temperature field of the air film flow in the GFB is governed by the Reynolds equation and the energy transport equation. Sim and Kim [9] present a 3-D energy transport equation coupled with the Reynolds equation for a compressible fluid flow, which is given as:

$$\frac{\partial}{\partial x}\left(\frac{\rho h^3}{\mu}\frac{\partial p}{\partial x}\right)+\frac{\partial}{\partial z}\left(\frac{\rho h^3}{\mu}\frac{\partial p}{\partial z}\right)=6U\frac{\partial}{\partial x}(\rho h) \tag{1}$$

$$\rho c_p\left(V_x\frac{\partial T}{\partial x}+V_y\frac{\partial T}{\partial y}+V_z\frac{\partial T}{\partial z}\right)=k_f\left(\frac{\partial^2 T}{\partial x^2}+\frac{\partial^2 T}{\partial y^2}+\frac{\partial^2 T}{\partial z^2}\right)+\left(V_x\frac{\partial p}{\partial x}+V_z\frac{\partial p}{\partial z}\right)+\mu\left[\left(\frac{\partial V_x}{\partial y}\right)^2+\left(\frac{\partial V_z}{\partial y}\right)^2\right] \tag{2}$$

, where p and T are hydrodynamic pressure and temperature of the air film flow, respectively. ρ is the air density, c_p is the specific heat capacity of the air at a constant pressure, V_i is the air film flow velocity (i=x,y,z), k_f is the thermal conductivity of the air, and μ is the dynamic viscosity of the air. The Reynolds equation is solved with the boundary conditions of the ambient pressure at all the side edges and the leading and trailing edges. The two governing equations become coupled using two variables of pressure and temperature by applying the ideal gas equation and the linear viscosity-temperature relation. They are solved iteratively until convergence [9]. Details on the formulation of the THD model with the Reynolds equation and energy transport equation, and the discretization of the energy transport equation for numerical simulations are detailed in Ref. [16].

The thermal boundary conditions for the energy transport equation are defined at the inlet, side edges and exit of the air film flow, as well as at the interfaces to the foil structure. The side leakage flows are pressure-driven and purely outgoing due to the ambient film pressure in the trailing edge region, resulting from the top foil detachment from the bump foil in the sub-ambient film pressure region [10]. It is assumed that the outgoing side and exit flows have large Peclet numbers, and thus, require no boundary condition [11]. In a relatively large space between the leading and trailing edges of the top foil, the mass and energy balances among the exit flow, side suction flows, and inlet flow yield the inlet boundary condition [9]. The side suction flow rate is identical to the side leakage flow rate due to the mass balance of the air film flow. Note that the side leakage flow rate is obtained from Reynolds equation. On the other hand, the thermal boundary conditions at the interfaces to the top foil and shaft require thermal models of the surrounding solid structures.

The backside surface of the top foil experiences either heat convection to the bump channels or heat conduction to the bump foil. The thermal boundary condition of the 3-D energy transport equation at the air film/top foil interface is defined by an equivalent thermal conductance including the top foil and either of the heat convection or conduction. Heat flux balances at the air film/top foil interface for the heat convection and conduction, respectively, yields:

$$k_f \left.\frac{\partial T}{\partial y}\right|_{y=0} = \frac{1}{1/h_T + 1/h_{T,conv}} \left(T|_{y=0} - T_{ch} \right) \tag{3}$$

$$k_f \left.\frac{\partial T}{\partial y}\right|_{y=0} = \frac{1}{1/h_T} \left(T|_{y=0} - T_{B1} \right) \tag{4}$$

, where T_{ch} is the bump channel temperature (=T_a), and T_{B1} is the bump summit temperature. h_T is the thermal conductance of the top foil in the cross-thickness direction ($h_T = k_T/t_T$, where k_T is the top foil thermal conductivity, and t_T is the top foil thickness). $h_{T,conv}$ is the heat transfer coefficients of the heat convection to bump channel. Presently, the top and bump foils are assumed to have an identical temperature at the contact surface, ignoring the thermal contact effects [13]. The heat convection on the top foil surface is natural without a forced cooling flow, and $h_{T,conv}$ is calculated from the natural heat convection model in Appendix A.

THERMAL MODEL OF BUMP FOIL

Figure 12 gives a thermal resistance model of a bump arc from a bump summit to a bump base with heat convections to bump channels at the bump arc center. The bump foil structure links the temperature fields of the air film/top foil to the bearing housing. Half the bump arc from its summit to the base is modeled as a thermal resistance of heat conduction along the arc. The heat convection on the bump surface is also modeled as a thermal resistance.

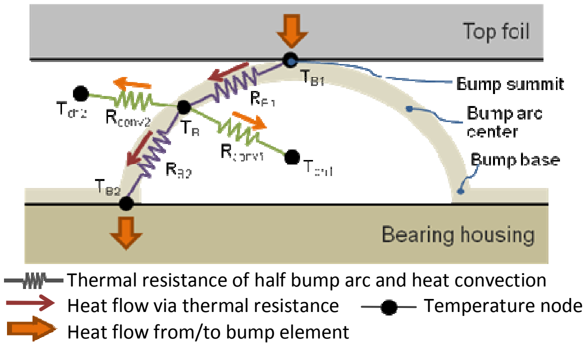

Fig. 12 Thermal resistance model of a bump arc from bump summit to base with heat convections to bump channels at bump arc center.

The bump summit temperature is associated to the bump base temperature by the thermal balance at the bump arc center, and given as:

$$Q_{B1} = Q_{B2} + Q_{ch} \tag{5}$$

, where $Q_{B1} = \dfrac{T_{B1} - T_B}{R_{B1}}$, $Q_{B2} = \dfrac{T_B - T_{B2}}{R_{B2}}$, $Q_{ch} = \dfrac{T_B - T_{ch}}{R_{conv}}$.

Q_{B1} and Q_{B2} are the heat flows via the thermal resistances of R_{B1} and R_{B2}, respectively. R_{B1} and R_{B2} are the thermal resistances from the bump arc center to the summit and the base, respectively, and $R_{B1}=R_{B2}=0.5l_B/k_BA_B$, where l_B, k_B, and A_B are the bump arc length from the summit to the base, the bump thermal conductivity, and the cross sectional area of the bump arc, respectively. T_{B1}, T_B and T_{B2} are the bump temperatures at the summit, center, and base, respectively. The Q_{ch} is the heat flow via the thermal resistance of R_{conv}, where $Q_{ch}=Q_{ch1}+Q_{ch2}$, and $R_{conv}= R_{conv1}+R_{conv2}$. R_{conv1} and R_{conv2} are the thermal resistances related to heat convection between bump and channel, and Q_{ch1} and Q_{ch2} are the heat flows via the thermal resistances of R_{conv1} and R_{conv2}, respectively. T_{ch1} and T_{ch2} are the adjacent bump channel temperatures in both sides of the bump arc, which are assumed as T_a thus $R_{conv1}=R_{conv2}$. The thermal resistance of the heat convection is defined as $R_{conv}=1/h_{B,conv}A_{conv}$, where A_{conv} is the bump surface area from the summit to the base, and $h_{B,conv}$ is the heat transfer coefficient of heat convection on the bump surface, and calculated from the natural heat convection model in Appendix A.

THERMAL MODEL OF SHAFT AND HOUSING

A rotating shaft in most turbomachinery has a significant axial heat conduction from one side to the other, e.g., from a turbine to a compressor in gas turbines. A few THD models consider the axial heat conductions along the shaft in Ref. [13] for GFBs or in Ref. [9] for tilting pad gas bearings. A radial heat conduction also needs to be taken into account when a considerable temperature variation occurs across the shaft shell thickness, e.g., a cooling stream flow supplied within the shaft. Presently, for more accurate prediction of physical system, test shaft is modeled with an axi-symmetric 2-D heat conduction in the axial and radial directions. Note that the shaft temperature along the circumference is assumed to be constant due to its high speed rotation and high thermal conductivity [9]. The bearing housing is also modeled as a 3-D heat conduction to consider detailed temperature variations, in particular for the circumferential direction. The relatively small wall thicknesses of the hollow shaft and the bearing housing compared to the other GFB dimensions rationalizes the use of the Cartesian coordinates.

The axi-symmetric 2-D heat conduction of a shaft in the cross-thickness and axial directions (y_R and z_R, respectively) is modeled as:

$$\frac{\partial^2 T_R}{\partial y_R^{\,2}} + \frac{\partial^2 T_R}{\partial z_R^{\,2}} = 0 \tag{6}$$

, where T_R is the shaft temperature. The axial boundary condition at the bearing side edges is either a temperature or heat flux given, and described as:

$$T_{R,z_R=z_0} = T_{given} \quad \text{or} \quad T_{R,z_R=z_0} + \frac{k_R}{h_{R,conv1}} \left.\frac{\partial T_R}{\partial z_R}\right|_{z_R=z_0} = T_a \tag{7}$$

, where z_0 is the axial boundary position (0 or L), and k_R and $h_{R,conv1}$ are the thermal conductivity of the shaft and the heat transfer coefficient of heat convection on the shaft side surface, respectively. Heat balance at the shaft/air film interface [9] yields:

$$-k_R \left.\frac{\partial T_R}{\partial y_R}\right|_{y_R=0} = \frac{1}{2\pi R}\int_{x=0}^{2\pi R} -k_f \left.\frac{\partial T}{\partial y}\right|_{y=t_f} dx \tag{8}$$

, where y_R has the origin at the shaft outer surface, t_f is the film thickness. At the interface to a hollow space inside the shaft, a heat convection or adiabatic boundary condition is applied depending on the shaft channel flow condition, and given as:

$$-k_R \left.\frac{\partial T_R}{\partial y_R}\right|_{y_R=t_R} = h_{R,conv2}\left(T_{R,y_R=t_R} - T_{ch,R}\right) \tag{9}$$

, where t_R is the shaft thickness, $T_{ch,R}$ is the shaft channel temperature, and $h_{R,conv2}$ is the heat transfer coefficient of heat convection on the shaft inner surface.

The bearing housing is modeled as a 3-D heat conduction, and the governing equation is given as:

$$\frac{\partial^2 T_H}{\partial x_H^{\,2}} + \frac{\partial^2 T_H}{\partial y_H^{\,2}} + \frac{\partial^2 T_H}{\partial z_H^{\,2}} = 0 \tag{10}$$

, where T_H is the bearing housing temperature. The heat transfer mechanism on the inner surface (the bump foil side) is similar to the backside of the top foil, i.e., the heat conduction to the bump foil or the heat convection to the bump channels depending on the bump contacts. Thermal boundary conditions on the side and outer surfaces are a temperature or heat convection coefficient given, depending on heat transfer conditions. The 1st order continuity of temperature is applied at the circumferential origin.

BOUNDARY CONDITIONS OF TEST GFB

Figure 13 presents the thermal domain of the test GFB and hollow shaft. The shaft surface exposed to the ambient air experiences strong forced heat convections due to rotor spinning, while the bearing housing is subject to natural or moderate forced heat convections. The THD model predicts all the temperature fields of the GFB system with a single shaft temperature measurement on the right side (TR_R). The model also accounts for the net thermal expansions of the GFB housing and hollow shaft. Note that the foil structure thermal expansion is neglected because its thickness is two orders of magnitude smaller than the bearing diameter. The radial thermal expansions are calculated using linear thermal expansion coefficients and predicted averaged temperatures. The centrifugal shaft growth is not considered because of the relatively low bearing numbers.

As illustrated in Fig. 13 and listed in Table 4, the thermal boundary surfaces comprise: 1) the inner surface (S6) and cross-sectional areas at the bearing edges (S7-8) of the hollow shaft, and 2) the outer surface (S11) and side surfaces (S9-10) of the GFB housing. The shaft model has a temperature boundary condition on S8, i.e., measured right shaft temperature (TR_R). Equivalent heat convection coefficients are defined on S6 and S7, such that the outgoing heat flows on S6 and S7 are identical to total heat convections on S4-6 and S1-3, respectively. The outer surface of S11 experiences natural heat convection. The side surfaces of S9-10 encounter a forced convection due to rotating flows around the shaft. The heat convection coefficient on each surface is calculated from a corresponding heat convection model of a rotating cylinder or a rotating disk from [12,14,15]. The rotating disk model is applied to the heat convection on the side surface of the GFB housing with 50% reduced values because the infrared thermometers besides the housing obstruct the rotating flows[1]. All the heat convection coefficients are calculated at the room temperature of 30 °C because all the measured temperatures were less than 70 °C, yielding negligible variations of thermo-physical properties of the ambient air. The thermal boundary conditions of the THD model and their heat convection models are summarized in Table 5. Details on the calculation of the heat convection coefficients are provided in Appendix A.

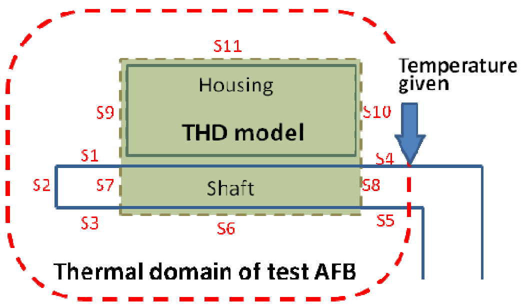

Fig. 13 Numerical domain of test GFB and shaft with denoted thermal model boundary conditions. See also Table 4.

Table 4. Notations for thermal boundary locations in Fig. 13.

Notation	Thermal boundary location
S1	Outer surface of shaft (left)
S4	Outer surface of shaft (right)

[1] The heat convection coefficient is an ad-hoc value for the present test rig setup with the test bearing housing which blocks (or disturbs) the rotating flows around the shaft.

S2	Side surface of shaft (left end)
S3	Inner surface of shaft (left)
S5	Inner surface of shaft (right)
S6	Inner surfaces of shaft (middle)
S7	Side surface of shaft numerical domain (left end)
S8	Side surface of shaft numerical domain (right end)
S9	Side surface of bearing housing (left)
S10	Side surface of bearing housing (right)
S11	Outer surface of bearing housing

Table 5 Thermal boundary conditions on test GFB housing and hollow shaft for THD model and applied heat convection models on boundary locations

Thermal BCs of GFB housing	
S9, S10	Forced convection approximated from the rotating disk model [14]
S11	Natural convection [12]
Thermal BCs of hollow shaft	
S6	Equivalent heat convection of S4, S5, and S6
S7	Equivalent heat convection of S1, S2, and S3
S8	Temperature given
Heat convection model	
S1, S4	Outer surface of rotating cylinder [14]
S3, S5, S6	Inner surface of rotating cylinder [15]
S2	Rotating disk [14]

MODEL PREDICTIONS COMPARED TO TEST MEASUREMENTS

Figure 14 shows predicted GFB temperatures at the bearing centerline for the shaft speed of 10 krpm with increasing static loads of 6 kg_f, 8 kg_f, and 10 kg_f. The predictions are compared to test measurements in Tables 2 and 3. In general, the predictions show good agreements to measured temperatures for both the nominal radial clearances of 70 μm and 40 μm. The predictions also describe well the temperature variations along the circumferential direction: approximately symmetric with respect to 180 deg (loading direction) for the nominal radial clearance of 70 μm. Note the shift in the predicted temperature peak from 180 deg to 225 deg by decreasing the clearance of 70 μm to 40 μm, which mimics the shift in the measured temperature peak. The model also predicts reasonably the overall temperature increases with increasing static loads.

For the shaft speeds of 5 krpm and 15 krpm and the nominal radial clearance of 70 μm, the THD model predicts lower temperatures than test data, in particular for 5krpm[2] in Fig. 15. However, the predictions depict the increasing differences between GFB temperatures at the loading (135 deg and 225 deg) and unloading (45 deg and 315 deg) zones as the shaft speed increases. In summary, the model predictions describes well the temperature rises of the GFB housing with increasing static loads and shaft speeds, the temperature variations along the circumferential direction, and change in the nominal radial clearance.

[2] Predictions for 5 krpm show larger differences from test data because of possible mixed lubrications at the low rotor speed.

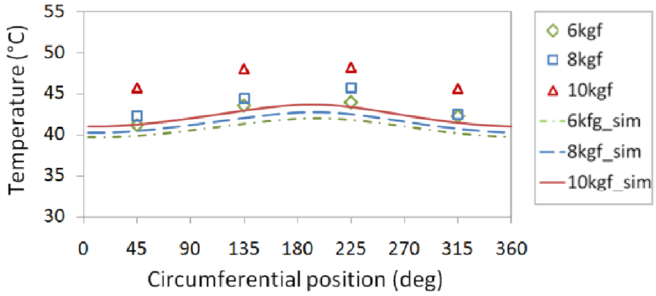

(a) Nominal radial clearance of 70 μm

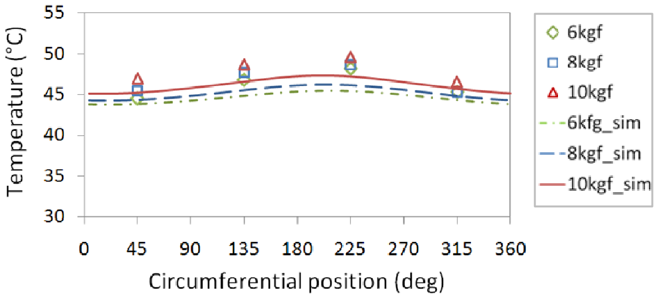

(b) Nominal radial clearance of 40 μm

Fig. 14 Predictions of GFB housing temperature at bearing centerline for shaft speed of 10 krpm with increasing static loads of 6 kgf, 8 kgf, and 10 kgf. Predictions compared to measurements in Tables 2 and 3. Nominal radial clearances of (a) 70 μm and (b) 40 μm.

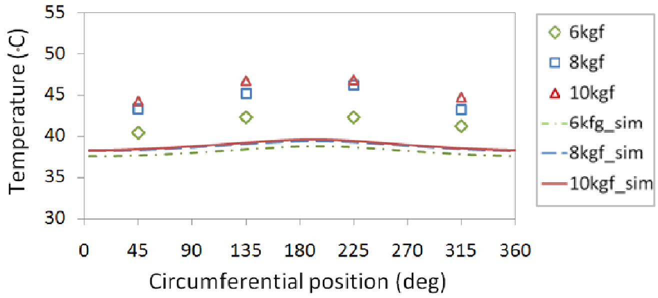

(a) Shaft speed of 5 krpm

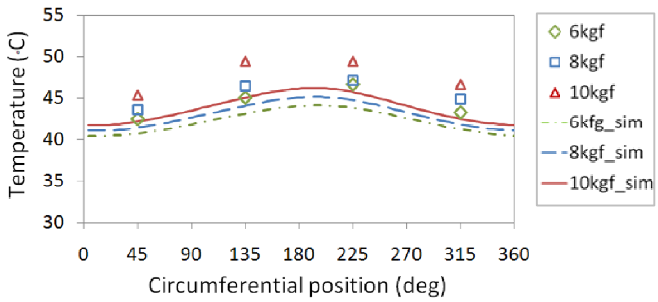

(b) Shaft speed of 15 krpm

Fig. 15 Predictions of GFB housing temperature at bearing centerline for shaft speeds of (a) 5 krpm and (b) 15 krpm with increasing static loads of 6 kg_f, 8 kg_f, and 10 kg_f. Predictions compared to measurements in Table 2. Nominal radial clearances of 70 μm.

Figure 16 presents predicted shaft temperature for the shaft speeds of 5 krpm, 10 krpm, and 15 krpm with increasing static loads of 6 kg_f, 8 kg_f, and 10 kg_f. The nominal radial clearance of test GFB is 70 μm. The predictions are compared to the measurements in Table 2. Note that for estimation of the shaft left end temperature (TR_L), the numerically predicted axi-symmetric shaft temperatures are averaged over the shaft shell thickness to obtain the axial temperature distribution. In general, the shaft temperatures in the bearing section increase with higher static loads for all the shaft speeds. The axial shaft temperature or thermal gradient becomes more significant with increasing rotor speed due to the increase in heat generation within the air film flow and stronger heat convection at the shaft free (left) end. The shaft left end temperature measured at a distance of ~10 mm from the housing is predicted using a linear extrapolation with a temperature slope at the bearing left edge. The temperature slope is highest at the top speed of 15 krpm. The estimated shaft left end temperatures are in good agreement with test data.

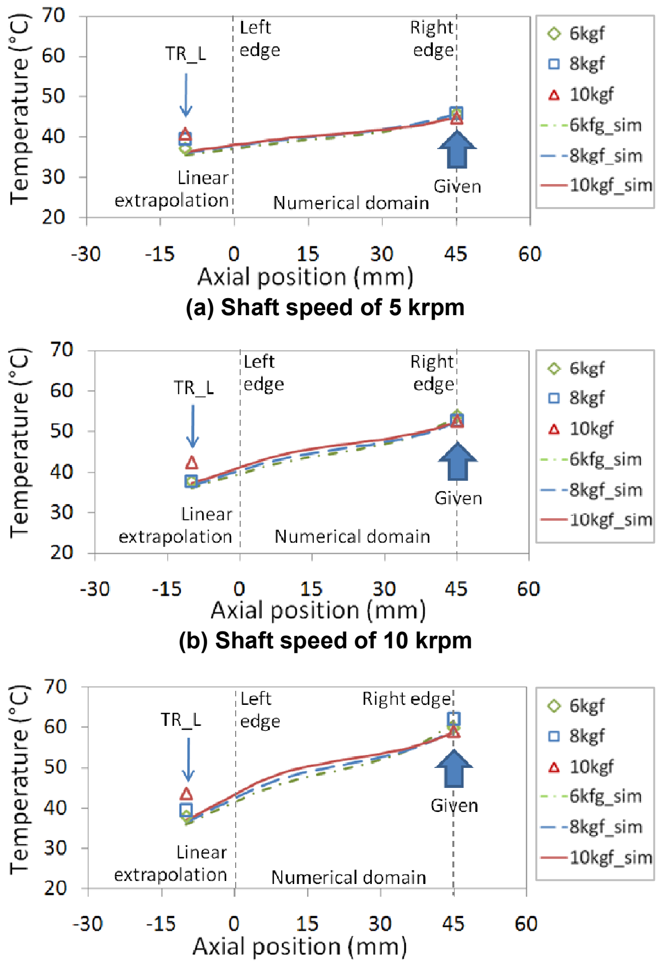

(a) Shaft speed of 5 krpm

(b) Shaft speed of 10 krpm

(c) Shaft speed of 15 krpm

Fig. 16 Predictions of shaft temperature at left end for shaft speeds of (a) 5 krpm, (b) 10 krpm, and (c) 15 krpm with static loads of 6 kg_f, 8 kg_f, and 10 kg_f. Predictions compared to measurements in Table 2. Nominal radial clearances of 70 μm.

CONCLUSION

The paper presents temperature measurements of a bump type GFB floating on a hollow shaft for various operating conditions. The hollow shaft is supported on two angular ball bearings and the test GFB is loaded upward via a metal wire. The bearing static load test is conducted for increasing shaft speeds of 5 krpm, 10 krpm, and 15 krpm with static loads of 6 kg_f, 8 kg_f, and 10 kg_f. Twelve thermocouples measure the outer surface temperatures of the test GFB at four angular locations of 45 deg, 135 deg, 215 deg, and 315 deg, and three axial locations of the bearing centerline and both side edges at each angle. Two infrared thermometers measure the outer surface temperature of the hollow shaft at the free (left) and supported (right) ends.

Test results show that the GFB housing temperatures increase as the shaft speed increases and as the static load increases. Particularly, temperatures in the loading zone (135 deg and 215 deg) are higher than those in the unloading zone (45 deg and 315 deg). The circumferential temperature distributions are approximately symmetric with respect to 180 deg (longing angle). Measured temperatures at the bearing centerline are higher than those at the side edges. In addition, reduction of the bearing radial clearance from 70 μm to 30 μm results in slight temperature rises.

Experimental test data benchmark GFB model predictions. The THD model of test GFB is developed via thermal models of the axi-symmetric heat conductions of the shaft, 3-D energy transport in the air film, the thermal resistance of the bump arc, and 3-D heat conduction in the GFB housing. The THD model predicts all temperature fields with a single shaft temperature measurement on the shaft supported (right) side. In general, the THD model predictions show good agreements to the measurements and describe well the temperature variations along the circumference. The temperature peaks at 135 deg and 225 deg revealed larger heat generations within the air film flow in the loading zone. However, all the predictions slightly underestimate the measurements, in particular for 5 krpm due to possible mixed lubrications at the low rotor speed. It is thought that the implementation of a thermal contact resistance [13] at the bump contacts to the top foil and bearing housing into the present THD model may improve the accuracy of the model predictions.

The predicted shaft temperatures in the bearing section increase with increasing static loads for all shaft speeds. The axial shaft temperature or thermal gradient becomes more significant with increasing rotor speed due to the increase in heat generation within the air film flow and stronger heat convection at the shaft free (left) end. The shaft left end temperatures predicted using a linear extrapolation are in good agreement with test data.

In summary, the present THD model predictions describe well the temperature rises of the GFB housing with increasing static loads and shaft speeds, the temperature variations along the circumferential direction, and change in the nominal radial clearance. In addition, the model predicts the axial temperature gradient along the shaft length in good agreement with test measurements.

ACKNOWLEGEMENT

This material is based upon the works supported by Korea Institute of Science and Technology (KIST) Research Projects: R&D on Power Generation and Energy Storage Technology for Tri-Gen System and Development of Micro Power Pack Technology for Long Distance Traveling E-Vehicles.

NOMENCLATURE

A	Area [m^2]
C_{nom}	Nominal radial clearance [m]
c_p	Specific heat capacity of air at constant pressure [J kg^{-1} K^{-1}]
h	Heat transfer coefficient [W/m^{2}K]
k	Heat conductivity [W/(m-K)]
L	Axial length of bearing [m]
l_b	Bump arc length from summit to base [m]
p	Gas pressure [Pa]
R	Radius [m] or thermal resistance [W/K]
U	Linear speed of rotor outer surface [m/s]
V	Velocity [m/s]
t	Thickness [m]
T	Temperature (K)
X, Y	Global coordinate of GFB [m]
x,y,z	Local coordinate of film, shaft, and housing [m]
ρ	Density of air [kg/m^3]
μ	Dynamic viscosity of air [Pa-s]

Subscripts

a	Ambient
B	Bump (or bump foil)
$conv$	Convection
ch	Bump channel
eq	Equivalent
f	Air film
H	Bearing housing
i	Inner
nom	Nominal
R	Rotor or shaft
T	Top foil
o	Outer

APPENDIX A

The heat transfer coefficients of natural heat convection are calculated from a heat convection model from Ref. [12], given as:

$$\mathrm{Nu_D} = 0.36 + \frac{0.518(\mathrm{Gr_D\,Pr})^{1/4}}{[1+(0.559/\mathrm{Pr})^{9/16}]^{4/9}}; \ \mathrm{Gr_D Pr} < 10^9 \qquad \text{(B.1)}$$

, where $\mathrm{Gr_D}$ is the Grashof number ($=\beta \Delta T g D^3/\nu^2$), and β, ΔT, g, D, and ν are the volumetric expansion coefficient, temperature difference to the ambient air, gravitational acceleration, outer diameter, kinematic viscosity, respectively. Pr is the Prandtl number. $\mathrm{Nu_D}$ is the Nusselt number ($=h_c D/k$), and h_c and k are the heat transfer coefficient and thermal conductivity, respectively.

Heat convection coefficients on the outer surface of the rotating shaft are estimated using a heat convection model for a rotating cylinder from [14], and given as:

$$\mathrm{Nu_D} = 0.133\ \mathrm{Re_D}^{2/3}\,\mathrm{Pr}^{1/3};\ \mathrm{Re_D} < 4.3\times10^5,\ 0.7 < \mathrm{Pr} < 670 \qquad \text{(B.2)}$$

, where $\mathrm{Re_D}$ is the Reynolds number ($=\Omega D_o^2/\nu$), and Ω and D_o are the rotating speed and outer diameter, respectively. For the inner surface, a heat convection model from [15] is employed and given as:

$$\mathrm{Nu_D} = 8.5101\times10^{-6}\ \mathrm{Re_R}^{1.4513};\ 1.6\times10^3 < \mathrm{Re_R} < 2.77\times10^5 \qquad \text{(B.3)}$$

, where $\mathrm{Re_R}$ is the Reynolds number ($=\Omega D_i^2/2\nu$; D_i is the inner diameter). For the side surface at the shaft free end, the heat convection coefficients are calculated from a heat convection model for a rotating disk [14], and given as:

$$\mathrm{Nu_r} = \frac{0.585\,\mathrm{Re}_r^{\ 0.5}}{0.6/\mathrm{Pr} + 0.95/\mathrm{Pr}^{1/3}};\ \mathrm{Re_r} < 2.4\times10^5,\ \mathrm{Pr} > 0.5 \qquad \text{(B.4)}$$

, where $\mathrm{Re_r}$ is the Reynolds number ($=\Omega R_d^2/\nu$, where R_d is the disk radius). $\mathrm{Nu_r}$ is the Nusselt number ($=h_c R_d/k$).

REFERENCES

[1] Howard, S., 2009, "Misalignment in Gas Foil Journal Bearings: An Experimental Study," ASME J. Eng. Gas Turbines Power, **131**(2), p. 022501

[2] Heshmat, H., Walowit, J. A., and Pinkus, O., 1983, "Analysis of Gas-Lubricated Foil Journal Bearings," ASME J. Tribol., **105**, pp. 647-655

[3] Radil, K., DellaCorte, C., and Zeszotek, M., 2007, "Thermal Management Techniques for Oil-Free Turbomachinery Systems," STLE Tribol. Trans., **50**, pp. 319–327.

[4] Dellacorte, C., 1998, "A New Foil Air Bearing Test Rig for Use to 700 °C and 70,000 rpm," STLE Tribol. Trans., **41**(3), pp. 335-340.

[5] Dellacorte, C., Lukaszewicz, V., Valco, M.J., Radil, K.C., and Heshmat, H., 2000, "Performance and Durability of High Temperature Foil Air Bearings for Oil-Free Turbomachinery," STLE Tribol. Trans., **43**(4), pp. 774-780.

[6] Radil, K. C., and Zeszotek, M., 2004, "An Experimental Investigation into the Temperature Profile of a Compliant Foil Air Bearing," STLE Tribol. Trans., **47**(4), pp. 470–479.

[7] Kim, T. H., Breedlove, A. W., and San Andrés, L., 2009, "Characterization of Foil Bearing Structure at Increasing Temperatures: Static Load and Dynamic Force Performance," ASME J. Tribol., **131**(4), p. 041703.

[8] Kim, T. H., and San Andrés, L., 2010, "Thermohydrodynamic Model Predictions and Performance Measurements of Bump-Type Foil Bearing for Oil-Free Turboshaft Engines in Rotorcraft Propulsion Systems," ASME J. Tribol., **132**(1), p. 011701.

[9] Sim, K., and Kim, D., 2008, "Thermohydrodynamic Analysis of Compliant Flexure Pivot Tilting Pad Gas Bearings," ASME J. Eng. Gas Turbines Power, **130**(3), p. 032502.

[10] San Andres, L., and Kim, T. H., 2010, "Thermohydrodynamic Analysis of Bump Type Gas Foil

Bearings: A Model Anchored to Test Data," ASME J. Eng. Gas Turbines Power, **132**(4), p. 042504.

[11] Patankar, S. V., 1980, Numerical Heat Transfer and Fluid Flow, McGraw-Hill, New York, Ch.5.

[12] Mills, A. F., 1999, *Heat Transfer*, Prentice Hall, New Jersey, pp. 362-363.

[13] Lee, D. and Kim, D., 2010, "Thermohydrodynamic Analyses of Bump Air Foil Bearings with Detailed Thermal Model of Foil Structures and Rotor," ASME J. Tribol., **132**, p. 021704.

[14] Mills, A. F., 1999, *Heat Transfer*, Prentice Hall, New Jersey, pp. 325-330.

[15] Seghir-Ouali, S., Saury, D., Harmand, S., Phillipart, O., and Laloy, D., 2006, "Convective Heat Transfer Inside a Rotating Cylinder with an Axial Air Flow," Int. J. Therm. Sci., **45**, pp. 1166–1178.

[16] Sim, K., 2007, Rotordynamic and Thermal Analyses of Compliant Flexure Pivot Tilting Pad Gas Bearings, Ph.D. Dissertation, Texas A&M University, ch. 5.

[17] Salehi, M., Swanson, E., and Heshmat, H., 2001, "Thermal Features of Compliant Foil Bearings—Theory and Experiments," ASME J. Tribol., 123, pp. 566–571.

[18] Le Lez, S., 2007, "Caracterisques Statiques Et Dynaniques Des Paliers A Feuilles," Ph.D. thesis, Universite De Poitiers, Poitiers, France.

[19] Feng, K., and Kaneko, S., 2008, "A Study of Thermohydrodynamic Features of Multiwound Foil Bearing Using Lobatto Point Quadrature," ASME Paper No. GT2008-50110.